




Local-Micro-Zone-Wise Time-Resolved Integrated Digital Image Correlation for Evaluating the Mechanical Properties of Welding Joints

Y. Li¹  · J. Zhao² · J. Zhou³ · Y. Yang⁴ · X. Huang^{5,6} · Z. Liu¹

Received: 23 February 2022 / Accepted: 8 August 2022
© The Society for Experimental Mechanics, Inc 2022

Abstract

The comprehensive determination of mechanical properties of heterogeneous objects such as welding joint remains challenging in various scientific fields. This paper develops a Local-micro-zone-wise Time-resolved Integrated Digital Image Correlation (LTIDIC) method, which can self-divide different regions of the material and get the multiple elastic–plastic parameters of each region through parameter inversion simultaneously, including elastic modulus, yield strength, hardening coefficient, and hardening exponent. First, the principle and process of the LTIDIC method are demonstrated, and the method of automatically dividing regions is introduced. Then, the reliability of the LTIDIC is analyzed and optimized, based on evaluating the influence of the correlation criteria, the area size, the noise type, and the number of pictures on the results of parameter inversion. Finally, a uniaxial tensile test was performed on the friction stir welding joint of aluminum alloy 6061T6 thin plate sample, and the distribution of multiple mechanical parameters was measured by the LTIDIC method. The results show that the modulus in the weld zone ranges between 30 and 70 GPa, with the lowest modulus in the thermo-mechanical affected zone and the highest modulus in the heat affected zone. The yield strength in the weld zone ranged from 75–115 MPa. The elastic modulus distribution shows an asymmetric W-shape, and the plastic parameters generally show a decreasing trend from the weld nugget to both sides. The feasibility and accuracy of the LTIDIC method were verified by comparing the consistency with the localized DIC method. The proposed method can obtain multiple elastic–plastic parameter distributions in different areas of material simultaneously through a single tensile experiment and provide important experimental data for the evaluation of mechanical properties of heterogeneous materials similar to welding joints.

Highlights

1. The developed LTIDIC method can obtain multiple elastic–plastic parameter distributions including elastic modulus, yield strength, hardening coefficient, and hardening exponent simultaneously through a single tensile experiment.
2. Automatically identify areas of heterogeneous materials with different mechanical properties.
3. The parameter inversion error is less than 1% by analyzing the factors that affect parameter identification. It can effectively reduce the influence of random noise on the inversion and improve the accuracy of the results.

Keywords Stir friction welding · DIC method · Automatic partition · Parameter inversion · Plasticity theory

Yiyang Li and Jiaye Zhao contributed equally to this work.

✉ Z. Liu
liuzw@bit.edu.cn

¹ School of Aerospace Engineering, Beijing Institute of Technology, Beijing 100081, People's Republic of China

² Institute of Flexible Electronics Technology of Tsinghua, 314006, Zhejiang, People's Republic of China

³ Beijing Institute of Structure and Environment Engineering, Beijing 100076, People's Republic of China

⁴ AECC Beijing Institute of Aeronautical Materials, Beijing 100095, People's Republic of China

⁵ State Key Laboratory of Nonlinear Mechanics (LNM), Institute of Mechanics, Chinese Academy of Sciences, Beijing 100190, People's Republic of China

⁶ School of Engineering Science, University of Chinese Academy of Sciences, Beijing 100049, People's Republic of China

Introduction

In the classic parameter inversion method, the test piece is usually a homogeneous material, that is, the material parameters of all areas of the test piece are the same, but in actual applications, the material properties of different areas of the test piece may be different, such as welding materials, composite materials, heterogeneous materials containing inclusions, etc. Taking the welding material of the friction stir welding process as an example, through microstructure observation [1], the area around the weld can be divided into weld nugget zone, thermo-mechanical affected zone, heat affected zone. The mechanical properties of the three sub-zones of the weld are different and significantly different from the base metal, which is affected by the welding process. Although hardness can be used as an indicator to characterize the degree of weakening of the mechanical properties of the welded joint [2], it is not sufficient to fully characterize the elastic–plastic parameters of the weld region and a hardness testing is required.

Digital Image Correlation (DIC) is a well-established, non-contact diagnostic technique that has been developed and applied in different materials and experimental environments [3–5]. In recent years, with the development of the DIC method, the mechanical properties of the heterogeneous materials such as complex rock mass [6], particle-type composites [7], and welded joints [8–10] have been extensively studied. Bai et al. [11] used the DIC method to calculate the stress–strain curves of different areas of laser-welded materials and measured the distribution of elastic–plastic properties of the materials. Li et al. [12] directly measured the distribution of the hardening index n with the help of the 3D-DIC method and used the inversion model method to obtain the distribution of the strength coefficient k . The current methods can characterize the parameter distribution of different areas of the weld by uniaxially stretching the test piece made of the sheet containing the weld area, but these methods all rely on the measurement accuracy of the strain in the DIC subset size. For one thing, when using the DIC method for non-uniform strain field measurement, the subjective choice of smoothing window size and filter size has a significant impact on the strain calculation results [13]. For another, the strain measurement accuracy of optical extensometers based on the DIC method can reach up to 2 microstrains, but this requires the equivalent gauge length of the material to be around 10,000 pixels [14]. For an ordinary CCD camera, when the gauge length is 450 pixels, the strain error is about 50 microstrains. [15]. When measuring welds where there are multiple areas to be measured locally, the gauge

length of each area is difficult to meet this requirement, which will further increase the strain measurement error and dispersion. The processing method of Bai [11] is to smooth the measured local strain data in the time dimension and use the least square method for fitting. Smoothing, filtering, and fitting are effective means to improve strain accuracy, but there are manual interventions in the relevant processes of these numerical calculations, which may affect the parameter identification results.

Through the above analysis, it is not difficult to find that the existing methods have the problem of uncontrollable accuracy in the measurement of heterogeneous material parameters. The main reason is the manual intervention in the strain calculation, that is, the secondary errors from displacement to strain may lead to the accumulation of errors in the parameter identification process.

To improve the accuracy of multi-parameter measurement of heterogeneous materials and reduce potential manual intervention errors, this paper proposes a Local-micro-zone-wise Time-resolved Integrated Digital Image Correlation (LTIDIC) method, which can simultaneously invert the parameters of the elastic–plastic model of welding joint through a uniaxial stretching experiment. The reliability of the LTIDIC method and the factors affecting the parameter identification results are investigated through numerical experiments with simulative speckle. The distribution of elastic–plastic parameters of aluminum alloy friction stir welded joints was inverted in combination with the automatic partitioning method. The feasibility and correctness of this method are verified by comparison with the calculation results of the localized DIC method [9]. The results show that the modulus of the thermo-mechanical affected zone is the lowest, while the modulus of the heat affected zone is the highest in the weld zone, showing an asymmetric W-shaped distribution. The stability of the distribution of the plastic parameters is not as good as the modulus, and the plastic parameters generally show a decreasing trend from the weld nugget to both sides.

Principle

Principles of LTIDIC

Compared with the classic integrated digital image correlation algorithm, the timing algorithm mainly uses the integration of the time dimension to effectively reduce the influence of errors such as random noise on the parameter inversion results [16]. In the quasi-static mechanical loading process, according to the assumption of constant gray level, the speckle image passively follows the deformation

of the material and moves, and the speckle deformation field has continuity in space and time, so the gray level of the image before and after the deformation satisfies:

$$f(x, t_0) = g(x - u(x, t), t) + r(x, t) \tag{1}$$

$$x = [x, y] \tag{2}$$

$$u = [u, v] \tag{3}$$

where $f(x, t_0)$ represents the gray distribution of the reference image (the unloaded speckle image of the specimen surface collected at the initial time t_0) in the image coordinate x , $g(x, t)$ represents the gray distribution of the deformed image at time t during the loading process, $u(x, t)$ represents the material displacement field at time t , as shown in Fig. 1, $r(x, t)$ represents the residual error caused by random noise, $g(x - u(x, t), t)$ represents the inverse affine transformation of the deformed image $g(x, t)$ back to the original undeformed image, $t = 1, 2 \dots, n$, n represents the number of acquired speckle images after deformation.

The material displacement field is determined by the loading boundary conditions and the material parameters. For this paper, the boundary condition is the uniaxial tension loading method, and the material parameter is the elastic–plastic parameters p_i of different regions Ω_i . In area Ω_i :

$$\begin{bmatrix} u \\ v \end{bmatrix} = \begin{bmatrix} \int \epsilon_{xx} dx + u_0 \\ \int \epsilon_{yy} dy + v_0 \end{bmatrix} \tag{4}$$

where ϵ_{xx} represents the transverse strain, ϵ_{yy} represents the axial (tension direction) strain, and u_0, v_0 represents the rigid displacement. The rigid displacement during the loading process can be directly solved by the DIC method.

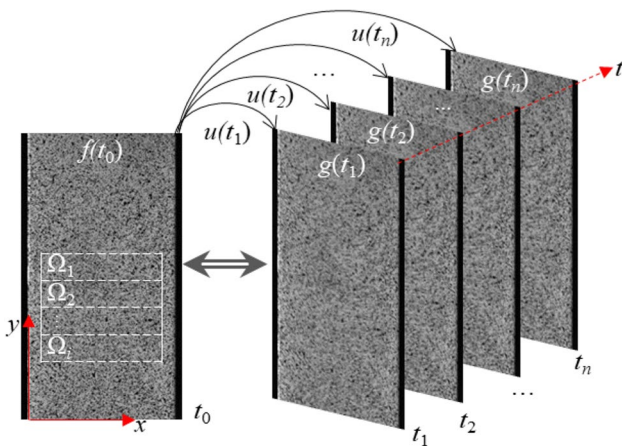


Fig. 1 Time series speckle image

According to Hooke's law, the standard test piece is in the uniaxial tensile test, the strain in the elastic phase satisfies:

$$\sigma^e = E_i \epsilon_{yy}^e \tag{5}$$

$$\epsilon_{xx}^e = -\nu_i * \epsilon_{yy}^e \tag{6}$$

where σ^e represents the stress in the elastic phase, E_i represents Young's modulus, ϵ_{yy}^e represents axial strain in the elastic phase, ϵ_{xx}^e represents transverse strain in the elastic phase, ν_i represents Poisson's ratio,

According to the simplified Johnson–Cook constitutive model [17], the strain in the plastic phase satisfies:

$$\sigma^p = A_i + B_i (\epsilon_{yy}^p)^{n_i} \tag{7}$$

$$\epsilon_{xx}^p = -0.5 * \epsilon_{yy}^p \tag{8}$$

where σ^p represents the stress in the plastic phase, A_i represents yield strength, B_i represents hardening coefficient, n_i represents hardening exponent, ϵ_{yy}^p represents axial strain in plastic phase, and ϵ_{xx}^p represents transverse strain in plastic phase.

During uniaxial stretching [8]:

$$\sigma(t) = F(t) / S(t) \tag{9}$$

$$S(t) = S_0 \exp(-\epsilon_{yy}) \tag{10}$$

where $F(t)$ represents the load at time t , $S(t)$ represents the cross-section area at time t , and S_0 represents the initial cross-sectional area. According to Eqs. (4–10), when the uniaxial stress $\sigma(t)$ is determined, the displacement $u(x, t)$ is determined by the elastic–plastic parameter $p_i = [E_i, \nu_i, A_i, B_i, n_i]$ of the material. Then, when p_i is the closest to the real material parameter, its determined displacement $u(x, p_i, t)$ makes (equation (1)) hold. Therefore, the objective function $C(p_i)$ can be constructed according to (equation (1)), and the parameter p_i can be solved by the optimization algorithm:

$$C(p_i) = \sum_t \sum_{\Omega_i} [g(\vec{x} - \vec{u}(\vec{x}, p_i, t), t) - f(\vec{x}, t_0)]^2 \tag{11}$$

Ignoring the influence of noise, the p_i with the smallest C is the closest to the real material parameters. This is a multi-parameter nonlinear optimization problem, which can be solved by linearizing the problem and iteratively, for example, using the Newton–Raphson algorithm [16]. The Newton–Raphson algorithm is an iterative update method based on the gradient correction term. The correction term can improve the initial guess. The correction term for the k th guess is:

$$\Delta p_{i,k} = -H^{-1}(p_{i,k})J(p_{i,k}) \tag{12}$$

$$J(p_{i,k}) = \partial C/\partial p_{i,k} = [\partial C/\partial E_i \ \partial C/\partial v_i \ \partial C/\partial A_i \ \partial C/\partial B_i \ \partial C/\partial n_i]^T \tag{13}$$

$$H(p_{i,k}) = J(p_{i,k})^T J(p_{i,k}) \tag{14}$$

where J is the Jacobian matrix, corresponding to the first-order partial derivative, and H is the Hessian matrix, which is a square matrix composed of the second-order partial derivatives of a multivariate function, which can be used to describe the local curvature of the function. For the case where there is a numerical analytical solution to the displacement field, an explicit functional relationship can be established between the unknown material parameter and the displacement field. In this case, the partial derivative is directly calculated through the functional relationship:

$$J(p_{i,k}) = \sum_t \sum_{\Omega_i} \nabla g \nabla u(g(\vec{x} - \vec{u}(\vec{x}, p_{i,k}, t), t) - f(\vec{x}, t_0)) \tag{15}$$

where ∇g represents the grayscale gradient of the image, which refers to the rate of change of the grayscale at a certain pixel position in the image in both the x and y directions (compared with adjacent pixels), and ∇u represents the first-order partial derivative of the displacement field to the material parameters.

For the implicit function relationship between the unknown material parameters and the displacement field, the partial derivative can be approximated by calculating the finite difference gradient:

$$J(p_{i,k}) = \frac{C((1 + \xi)p_{i,k}) - C(p_{i,k})}{\xi p_{i,k}} \tag{16}$$

where ξ represents iteration parameters and its value affects the speed of iterative convergence to a certain extent.

At this point, all the conditions for resolving the update of material parameters are in place. Run the generated iterative process until convergence is met. The convergence criterion is usually used:

$$\|\Delta C(p_{i,k})\| \leq 1e - 5 \tag{17}$$

or

$$\|\Delta p_{i,k}\| \leq 1e - 3 \tag{18}$$

LTIDIC Algorithm Flow

During the uniaxial stretching process of the welding test piece, each different area satisfies the series relationship. Before the test piece is necked, the axial strain is not

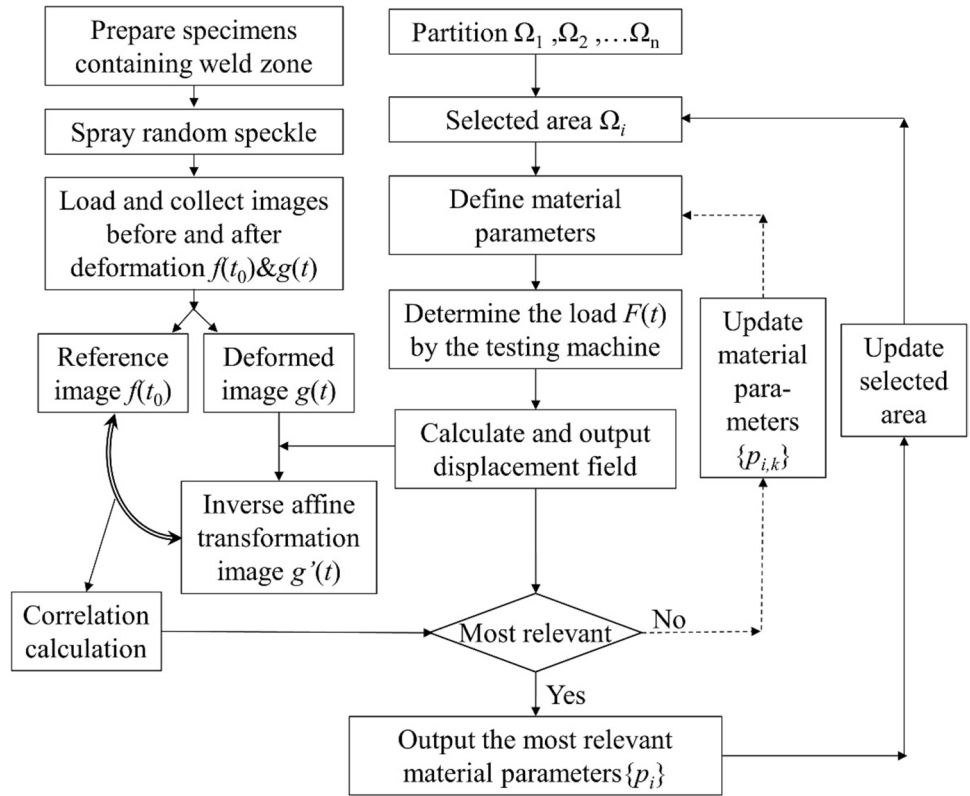
greater than 0.02, and the transverse strain is less than 0.001. It can be considered that the uniform uniaxial tensile stress is satisfied in each area, when the influence of the lateral deformation on the uneven distribution of the stress field is ignored [11], the force acting on each area is equal to the load of the testing machine. Therefore, the inverse solution of the material parameters can be performed separately for different areas. Here, the reason for not solving all regions at the same time is the complexity of solving the problem increases exponentially with each additional variable. Solving the parameters of all regions at the same time requires a lot of computing power and is difficult to converge. Therefore, when characterizing the elastic-plastic parameters of different areas of the weld, the traditional I-DIC method based on the overall image has great drawbacks. The LTIDIC algorithm proposed in this paper draws on the idea of the sub-region DIC method, considers the constraints of time and space continuity, and gradually inverts the constitutive model parameters of materials in different regions by automatic partition.

The algorithm flow is shown in Fig. 2, the specific steps are:

- ① Prepare uniaxial tensile test specimens containing weld zone, and spray speckle on the surface of test specimens;
- ② Apply a tensile load to the specimen, and take a speckle image of the specimen surface at the same time;
- ③ Use the automatic partition method developed in Section 2.3 to divide areas of the test piece;
- ④ Select the area and give the initial parameters of the material in the selected area;
- ⑤ Calculate the displacement field at different times in the selected area according to the initial value of the material and the Eqs. (4–10);
- ⑥ Perform inverse affine transformation on the deformed image according to the displacement field at different moments to obtain the constructed undeformed image;
- ⑦ Perform correlation operations on the undeformed image constructed by inverse affine transformation and the real shot reference image according to (equation (11)) to obtain the correlation function value;
- ⑧ Determine the convergence of the correlation function value, if it converges, proceeds to step ⑩, if it does not converge, proceeds to step ⑨;
- ⑨ Update the initial value of the material according to (equation (12–16)), and repeat steps ⑤–⑧
- ⑩ Update the selection and repeat steps ④–⑨.

The core of the LTIDIC algorithm lies in how to achieve the precise division of different regions accurately and

Fig. 2 LTIDIC algorithm flow chart



quickly, and the following will introduce the method of automatic region division.

Automatic Partition Method

The principle of the automated partition method is to identify the area boundaries of different materials on the test piece based on the difference in the response under specific loads. In the process of uniaxial stretching of a homogeneous material, before the specimen is necked, the displacement field on the surface of the specimen within the gauge length changes uniformly, and the strain at each point is theoretically equal. But for non-homogeneous materials, the displacement field on the surface of the specimen changes non-uniformly, and there are certain differences in strain in different regions. Therefore, the automatic partition method needs to first obtain the displacement and strain responses, and then analyze the response characteristics at the boundary, and find the appropriate response characteristics as the boundary judgment criterion. In this section, for the uniaxial tensile test of heterogeneous materials, a model of three materials stretched in series was developed is established to analyze the boundary judgment criteria of automatic partitions by numerical methods, as shown in Fig. 3.

Assuming that the horizontal widths of the three materials are equal, the axial lengths are 100 pixels, 50 pixels, and

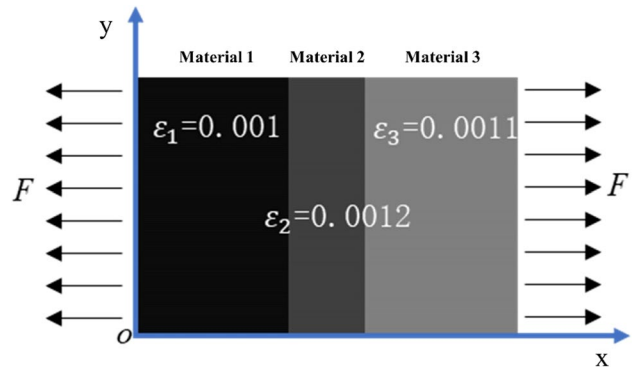


Fig. 3 Three-material series stretching model

100 pixels respectively. Under a certain fixed unidirectional force F , due to the different stiffness of the three materials, the axial strain is 0.001, 0.0012, and 0.0011 respectively. Ignoring the deformation in the y -direction, calculate the displacement in the x -direction according to Fig. 3.

Calculate the displacement, strain, first-order derivative of strain, and second-order derivative of the strain of each pixel in the x -direction. The relative values are shown in Fig. 4. In Fig. 4, in order to unify the coordinate axes, the results are translated and zoomed without affecting the regularity. It can be seen from the figure that at the boundary of the two materials in series, the displacement

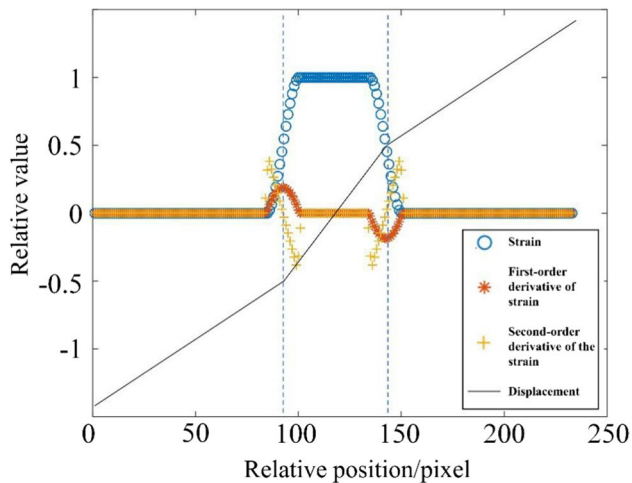


Fig. 4 Displacement, strain, and strain derivative of the three-material series tensile model

is the segmental inflection point, the strain is the midpoint of the gradual change, the first derivative of the strain is the extreme point, and the second derivative of the strain is equal to zero. Ideally, these results can be used as the basis for dividing the area. However, in the actual measurement of the weld, the displacement field is asymptotically curved, and it is difficult to divide the different areas according to the displacement field. Therefore, the extreme point of the first derivative of strain and the zero point of the second derivative of strain can be used as the basis for partition. Numerically, the sign of the second derivative of strain in the same connected region is the same, and rapid regional differentiation can be realized by binarizing the second derivative of strain with 0 as the boundary.

It should be pointed out that the material parameters of the weld area are gradual. The material area division here is to divide materials with similar parameters into the same area, and the material parameters with large differences are divided into different areas.

Reliability analysis and optimization of LTIDIC

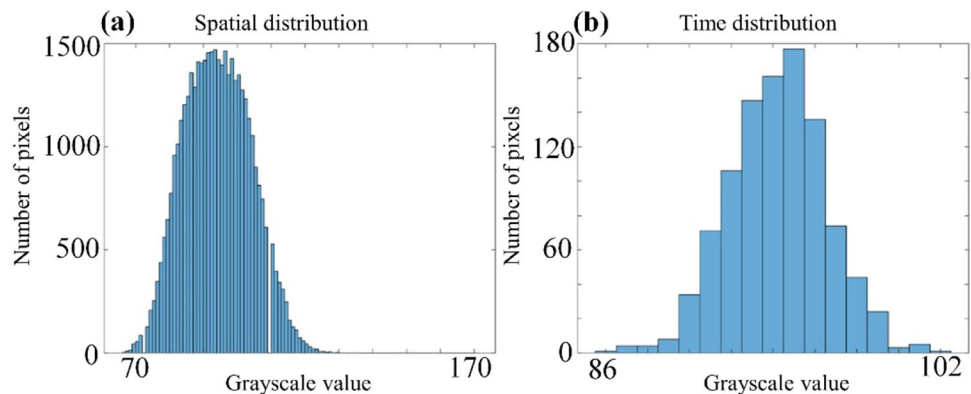
The numerical simulation experiment refers to the welding parameters of aluminum alloy and selects a set of parameter combinations: $E = 65$ GPa, $\nu = 0.3$, $A = 100$ MPa, $B = 300$ MPa, $n = 0.3$. Then select the maximum load $F_{max} = 9.6$ kN according to the experimental results, the gauge length of the test piece $L = 100$ mm, the plate width $b = 20$ mm, the plate thickness $L = 3$ mm, and the sampling frequency during the experiment is 10 fps. Calculate the theoretical displacement field at different times of uniaxial stretching. Then, the deformed speckle images at different moments are simulated according to the displacement fields at different times, and the image size is 801×801 pixels. Finally, parameter inversion is carried out using different correlation criteria, area size and the number of pictures. In each case, 50 separate inversions are performed. Statistical analysis of the inversion results can guide algorithm optimization.

Noise Analysis and Simulation

The noise mainly involved in the experiment includes image noise and strain noise. Image noise refers to unnecessary or redundant interference information in the image data. Strain noise refers to the sudden change of strain caused by the pores and vibration of the loading system.

The camera used in the experiment is a Daheng Mercury series CMOS camera with a resolution of 1944×2596 pixels. The mentioned camera was used to continuously collect 1000 pictures of white cardboard and collect the noise information of the images for analysis. Due to the influence of uneven illumination and camera noise, the gray information collected by the camera is not exactly the same. Figure 5 plots the gray distribution histograms (spatial distribution) of different pixel areas on the target surface at the same time

Fig. 5 Gray distribution histogram



and the gray distribution histograms (time distribution) of the same pixel at different times. It can be seen that both spatially and temporally, the grayscale distribution of the image satisfies the normal distribution, and the image noise type belongs to Gaussian noise. Spatially, the variance of image grayscale is 9.78, and temporally, the variance of image grayscale is 2.23.

The reason why the spatial variance is larger may be that the illumination is not completely uniform, while the temporal variance is almost entirely due to the image noise caused by the camera signal acquisition process.

Through the above analysis, this section uses Gaussian noise with a mean value of 0 and a variance of 2.23 as image noise to analyze the algorithm. Figure 6 shows the collected image noise and the simulated image noise. It can be seen that the simulated image noise is consistent with the actual situation, which makes the numerical experiment closer to the real situation.

Even if the same target is measured twice in a row under very strict conditions, the strain data collected at the same location may be different, which is especially obvious in the case of small deformation. According to the literature [18], the formula for adding strain noise is:

$$\epsilon'_{ij} = \epsilon_{ij} \cdot (1 + r_{nsr}\eta) \tag{19}$$

where ϵ_{ij} and ϵ'_{ij} respectively represent the strain before and after adding noise, η represents the random number distributed normally in the interval (0,1), and r_{nsr} represents the signal-to-noise ratio. The range of r_{nsr} for adding strain noise in the literature is (0.01%-0.09%) and (1%-10%). Due to limited conditions, it is hard to accurately evaluate the level of strain noise. This section r_{nsr} is taken as 1%, which is the critical point of low noise signal ratio and high noise signal ratio in the literature. And in subsequent numerical experiments, if there are no special instructions, only image noise is added.

Analysis and Discussion of Numerical Simulation Experiment Results

The noise is random, and the parameter inversion results are discrete. Therefore, in order to more accurately evaluate the influence of correlation criteria, area size, noise type, and the number of pictures on parameter errors, each combination of variables mentioned above requires multiple numerical simulations. Statistical methods are used to analyze the influence of variables on the accuracy and dispersion of parameter inversion.

(1) Error analysis of LTIDIC method for different parameter identification

Under the same noise level, the parameter inversion method has different recognition errors and dispersion degrees for different parameters. In this section, 50 numerical simulation experiments will be performed on different parameters respectively, and the error distribution of parameter inversion under the same correlation criteria, the same sub-region size, different noise types, and different number of pictures will be counted.

The inversion results of the numerical simulation experiments for different parameters at the same level of image noise are shown in Fig. 7. It can be seen that for the plasticity parameter $A/B/n$ of the material, the inversion errors are all within 1%, even with a small number of pictures. As for the modulus and Poisson's ratio, the error and dispersion decrease as the number of pictures increases. The dispersion of Poisson's ratio is greater than the dispersion of modulus in the case of the same number of pictures. It can be inferred that under the same level of image noise, the greater the influence of material parameters on deformation, the smaller the error and dispersion of the parameter inversion results.

Under the same level of strain noise, the inversion results of numerical simulation experiments with different parameters are shown in Fig. 8. It can be seen that for the plastic parameter $A/B/n$ of the material, even if the number of

Fig. 6 Histogram of image noise distribution

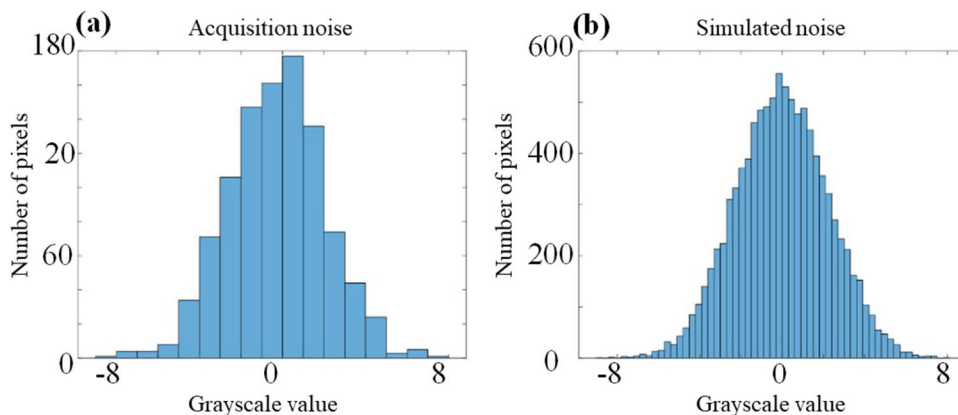


Fig. 7 The relationship between the relative errors of different parameters and the number of pictures under image noise: (a) Young's modulus; (b) Poisson's ratio; (c) yield strength; (d) hardening coefficient; (e) hardening exponent

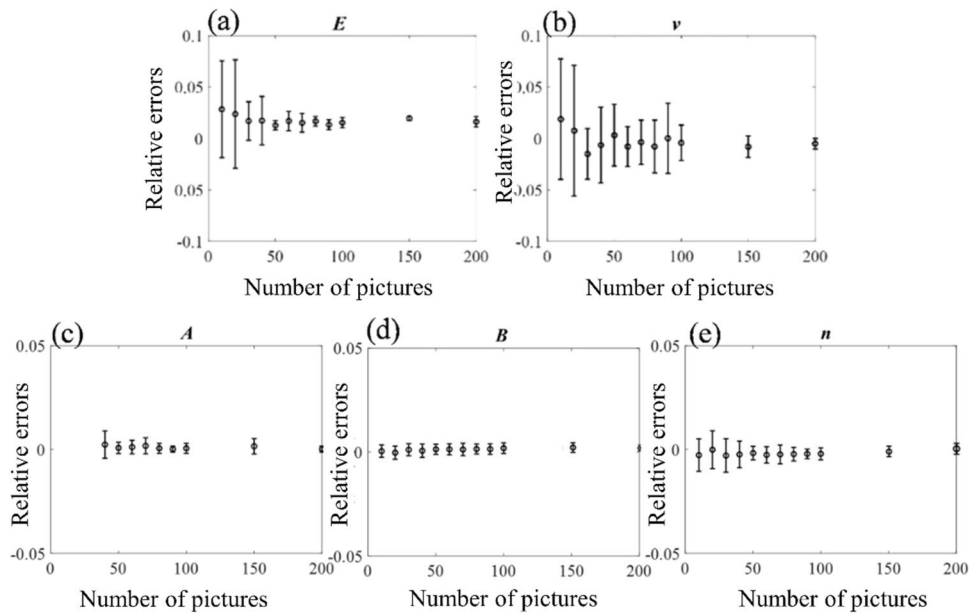
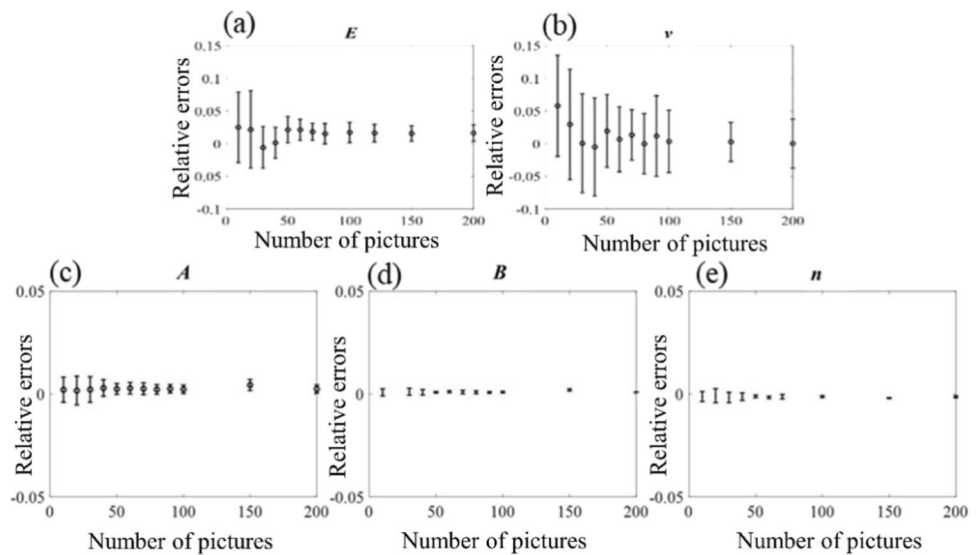


Fig. 8 The relationship between the relative error of different parameters and the number of pictures under strain noise: (a) Young's modulus; (b) Poisson's ratio; (c) yield strength; (d) hardening coefficient; (e) hardening exponent



pictures is small, the inversion error is all within 1%. As for the modulus and Poisson's ratio, the error and dispersion decrease as the number of pictures increases, and the overall rule is similar to image noise. The difference is that the dispersion of B and n under strain noise is lower than that under image noise, while the dispersion of E and ν under strain noise is higher than that under image noise. Especially for ν , in the presence of strain noise, the dispersion is very large. Strain noise has greater interference with elastic parameters, but less interference with plastic parameters. Combining the degree of influence of elastic–plastic parameters on deformation, it can be inferred that in the case of small deformation, the effect of strain noise on the parameter inversion

accuracy is greater than image noise, and in the case of large deformation, the effect of image noise is greater than strain noise.

(2) Error analysis of LTIDIC method for different correlation criteria

In the sub-area DIC method, different correlation functions are similar [19], which is also applicable to the LTIDIC algorithm. However, for specific problems, the anti-interference performance of different correlation functions is not the same. For the sub-area DIC method, most of the current zero-normalized sum-of-squared difference (ZNSSD)

correlation criteria is used, and for the I-DIC method, the least sum-of-squared difference (SSD) correlation criteria is commonly used. Here, the correlation criteria of SSD and ZNSSD will be selected as the objective function for parameter inversion. The specific formulas are Eq. (20) and Eq. (21).

$$SSD : C(p_i) = \sum_t \sum_{\Omega_i} [f(\bar{x}, t_0) - f(\bar{x} + \bar{u}(\bar{x}, p_i, t), t)]^2 \quad (20)$$

$$ZNSSD : C(p_i) = \sum_t \sum_{\Omega_i} \left(\frac{\bar{f}_i(\bar{x}, t_0)}{\sqrt{\sum \bar{f}_i^2(\bar{x}, t_0)}} - \frac{\bar{f}_i(\bar{x} + \bar{u}(\bar{x}, p_i, t), t)}{\sqrt{\sum \bar{f}_i^2(\bar{x} + \bar{u}(\bar{x}, p_i, t), t)}} \right)^2 \quad (21)$$

$$\bar{f}_i = f_i - \frac{1}{n} \sum_{i=1}^n f_i \quad (22)$$

Since the error of the parameter $A/B/n$ is small, the error of parameter E is selected to compare different related criteria. In this section, 50 numerical simulation experiments are conducted for parameter E respectively, and the error distribution of parameter inversions with different correlation criteria, different region sizes, and the number of images is counted. Figure 9 and Fig. 10 compare the mean value and dispersion of the parameter inversion errors of the two related criteria respectively. In the legend, A represents SSD, B represents ZNSSD, and the number represents the size of the sub-area (unit: pixels). The x-axis represents the number of pictures used to calculate the correlation function. For example, B50 means that the area is 50×50 pixels, using SSD criteria for parameter inversion. Overall, the average error of SSD is smaller, while the error dispersion of ZNSSD is smaller. The reason why the average error of ZNSSD is large may be that it is not sensitive to the linear change of

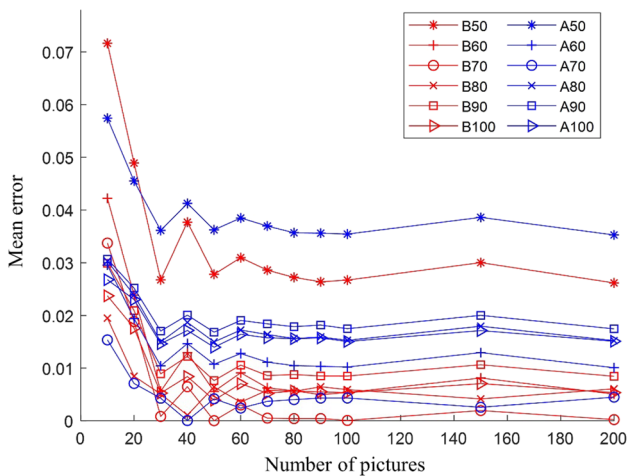


Fig. 9 Mean error comparison of parameter inversion results for SSD and ZNSSD correlation criteria

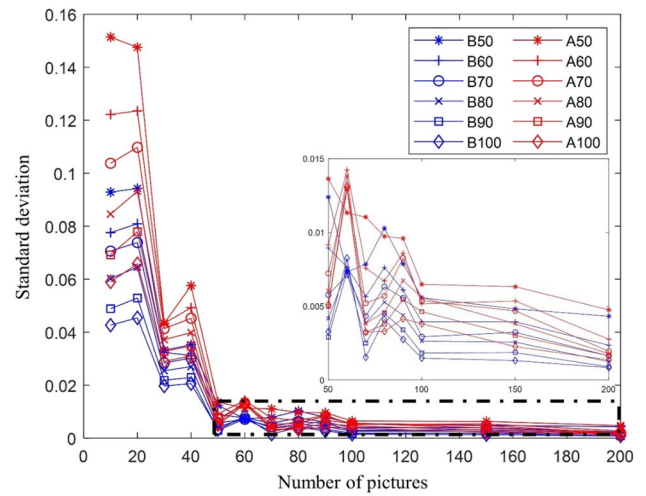


Fig. 10 Standard deviation comparison of parametric inversion results for SSD and ZNSSD correlation criteria

gray level. This paper mainly reflects on the uniaxial stretching experiment. According to the material parameters, the gray change of the surface of the specimen is a linear change.

(3) Error analysis of the LTIDIC method for different local area size

Section 2.3 introduces the method of automatic partition, but for the weld, the parameter distribution is gradual, and the divided area can only roughly divide the area with large parameter differences, and there are still parameter differences in each large area. It is necessary to discuss the inversion results of parameters with limited resolution in a limited area

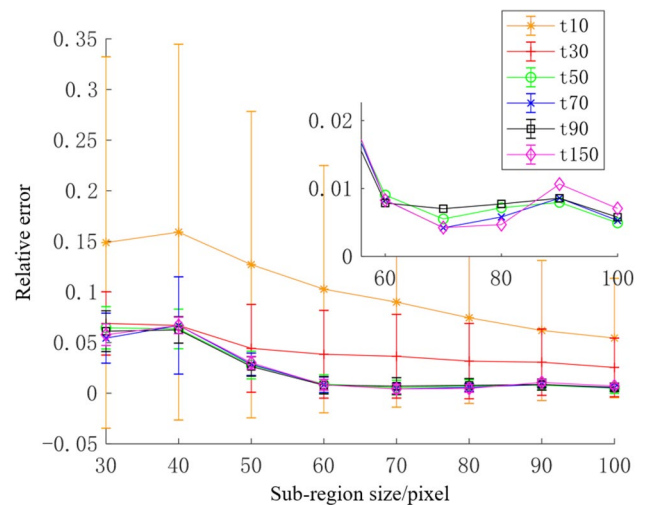


Fig. 11 Error comparison of different image sub-region sizes, the number in the legend indicates the number of pictures

to accurately characterize the distribution of parameters. Figure 11 is the error bar graph of the parameter inversion of E under different sub-region sizes given by the numerical simulation experiment. As the size of the sub-region increases, the average relative error gradually decreases and tends to converge. When the image sub-region is larger than $50 \text{ pixels} \times 50 \text{ pixels}$, the average error is less than 5%, and when the image sub-area is larger than $60 \text{ pixels} \times 60 \text{ pixels}$, the mean error converges. It can be seen from the partially enlarged view that the error is the smallest when the image sub-region is $70 \text{ pixels} \times 70 \text{ pixels}$, which shows that under the interference of image noise, oversampling may cause the error to increase.

(4) Error analysis of LTIDIC method for different numbers of pictures

In the time series parameter inversion method, the number of pictures depends on the loading speed and the frame rate of the camera. The number of pictures not only affects the calculation efficiency but also affects the accuracy of the parameter inversion. It can be seen from Fig. 9 that, as the number of pictures increases, the mean error gradually decreases, and when the number of pictures is greater than 50, it tends to converge. It can be seen from Fig. 10 that, as the number of pictures increases, the dispersion of the mean error gradually decreases. In order to more clearly and directly compare the influence of the number of pictures on the parameter inversion error, the data of the SSD-related criteria is selected, and the error bar graph (Fig. 12) is drawn. It can be seen from Fig. 12 that the mean value of the parameter inversion error gradually converges as the number of pictures increases. The distribution range of the error gradually decreases as the number of

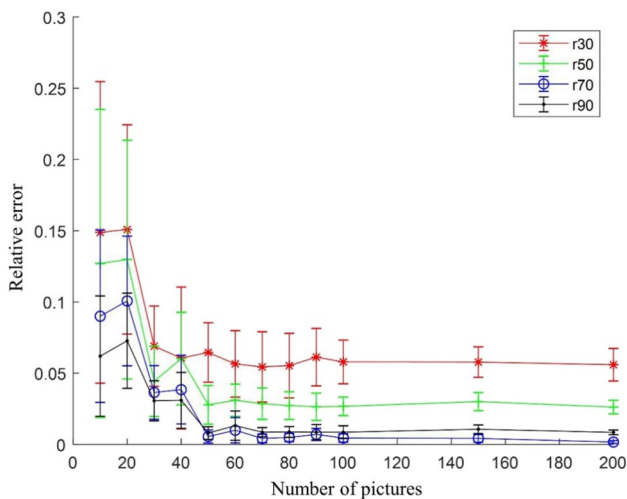


Fig. 12 Error comparison of different numbers of pictures, the number in the legend indicates the size of the sub-area

pictures increases, and the degree of convergence is related to the size of the sub-region.

Through the above numerical experimental results, the following relevant conclusions can be drawn: in the case of small deformation, the influence of strain noise is greater than image noise; LTIDIC method to achieve accurate parameter inversion (error less than 5%) needs to ensure that the image sub-area is greater than $50 \times 50 \text{ pixels}$, and the number of pictures is greater than 30; oversampling can reduce the dispersion, but it does not significantly improve the accuracy of parameter inversion, and it may increase the error. The diameter of speckles (in pixels) is about 4 and the step size is 5, based on the research on improving the accuracy of DIC method [20, 21]. When the size of the sub-region is limited, the method to further improve the accuracy (with an error of less than 1%) of the LTIDIC method is to collect an appropriate number of pictures, and then combine 50 groups of samples (In this case, 50 groups were used) through random sampling, the number of pictures in each group is 60, and then the SSD criterion is applied to elastic parameters inversion, and the average value of the 50 groups of samples is calculated. It is recommended to use the ZNSSD related criteria when the number of pictures is limited, because in the case that the calculation of the average error cannot be achieved, the dispersion of ZNSSD is smaller, which can ensure the accuracy and stability of the parameter measurement results.

Uniaxial Tensile Test of the Weld Joint

Specimen Preparation

The size of the sample with a friction stir welding area in this paper is shown in Fig. 13. The base material is aluminum alloy 6061T6, the modulus is 60GPa, and the yield strength is 250 MPa. The sample was cut from stir friction welded thin plate of aluminum alloy 6061T6 and the plate thickness is 3 mm. The processing parameters are shown in Table 1.

The direction and zone division of friction stir welding are shown in Fig. 14. Normal direction indicates the normal direction of the sheet and Longitudinal direction

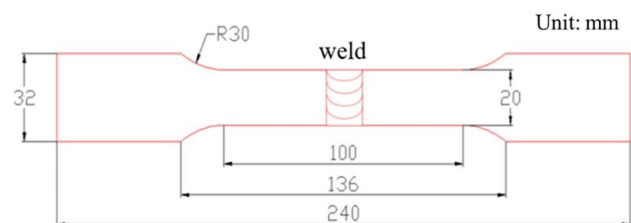


Fig. 13 Friction stir welding specimen

Table 1 Friction stir welding parameters

Welding speed	Rotational speed	Shaft shoulder	stirring pin	plunge depth	Tilt angle
300 mm/min	1200 rpm	10 mm	2.8 mm	2.8 mm	2.5°

indicates the direction perpendicular to the weld in the plane of the sheet. AS represents the advancing side when the friction stir welding shaft shoulder rotates, and RS represents the retreating side. Generally, the vicinity of friction stir welding joints can be divided into WN (Weld Nugget), TMAZ (Thermo-Mechanical Affected Zone), and HAZ (Heat Affected Zone) according to the microscopic results [18]. The TMAZ is located near the shaft shoulder, and its microstructure has obvious rotating textures. However, some studies have carried out a more detailed division of the welding area. The macro observation of the joints revealed a ‘bowl’ shaped weld nugget without any discontinuity and defects. According to different microstructures of the lap welded cross-section with respect to the shoulder and pin positions, Ghosh divides the solder nugget into three areas, including a mixed zone consisting of characteristics of adjacent areas [22]. The mechanical properties of WN, TMAZ, and HAZ are different, but the mechanical properties of the welding zone change continuously, so this paper divides the area according to the changes in mechanical properties.

Uniaxial Tension Testing

The uniaxial tensile test is used to obtain the mechanical properties of the aluminum alloy friction stir welding joints, the stretching direction is the same as the longitudinal direction in Fig. 14, and there are speckles on the surface of the specimen. The camera was used to take pictures during the stretching experiment, and the 2D-DIC method is used to obtain the deformation and strain information at the joints,

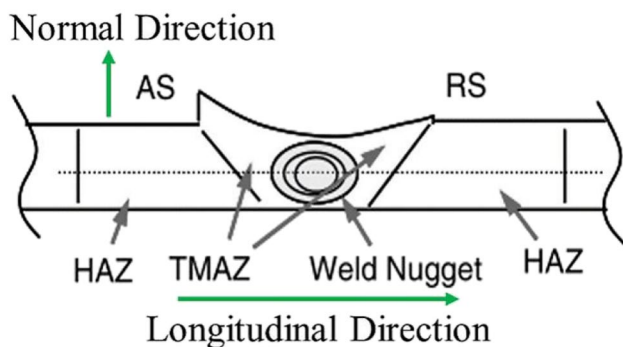


Fig. 14 Friction stir welded joint

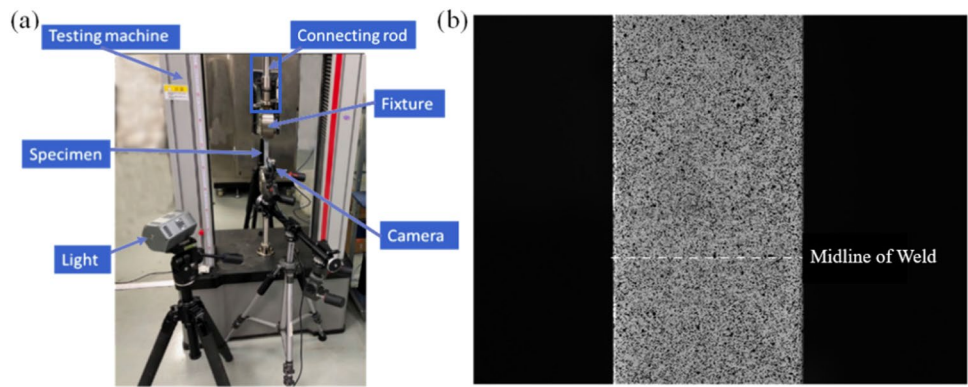
the optical axis of the camera is parallel to the normal direction in Fig. 15. In this experiment, the loading speed is 1 mm/min, the image acquisition is 1fps, and the image resolution is 2448 × 1942 pixels.

Results and analysis

The area around the weld is selected as the area of interest, and the strain field in the y-direction corresponding to a load of 5kN (the load at which the weld material has yielded) is calculated by the Ncorr [23] (an open-source 2D digital image correlation MATLAB), which is used as the basis for the division of the weld zone. When the DIC method calculates the strain, the selected parameters are as follows: the size of the sub-region is 45 × 45 pixels, the distance between the center points of the sub-region is 5 pixels, and the size of the strain smoothing window is 15 × 15 pixels. The strain calculation result is shown in Fig. 16a, the white dashed line indicates the stretching direction. The gradient change of the strain field is not completely perpendicular to the tensile direction due to the non-parallelism of the weld itself. Taking the average value of the strain field along the vertical direction of the stretching direction, the weld area can be divided into 5 different areas through the automatic zoning method developed in Section 2.3, as shown in Fig. 16b. It can be seen from the strain field that there are obviously 2 high-strain regions and 3 low-strain regions, a total of 5 regions. The calculation area includes the WN, TMAZ, and a part of HAZ. By calculating the second derivative of the strain, the changes in its mechanical properties can be identified to achieve a more accurate regional division.

In order to show the change of the material parameters along the vertical weld direction, 14 points on the white dashed line are selected as the center of the area for parameter inversion. According to the results of the automatic region division, each region is about 100 pixels long in the stretching direction, therefore, the image sub-region is selected as 50 × 50 pixels. According to the analysis in Section 3, the number of images needs to be greater than 30 to ensure that the average error is less than 5%. In the middle part of the loading process, 130 pictures with stress in the range of 50–160 MPa are input into the LTIDIC algorithm program to invert the parameters. When the stress is low, the testing machine used uses a long connecting rod as shown in Fig. 15a, so there is a larger pore, which causes the rigid body of the test piece to rotate larger, which has a great impact on the parameter inversion. Under high stress, the specimen necks down and no longer meets the assumption of a uniform stress field. Therefore, the pictures with the stress in the range of 50–160 MPa are selected, and the elastic–plastic parameter distribution of the weld zone is identified by the LTIDIC algorithm. Because the lateral

Fig. 15 Experimental setup and speckle image: (a) Experimental device; (b) Speckle image



deformation in the experiment is too small and is seriously affected by noise, it is hard to accurately obtain the Poisson's ratio distribution of the material, so the Poisson's ratio of the material is assumed to be 0.3 in the inversion process.

The inversion parameter distribution results are shown in Fig. 17, in which Fig. 17a marks the approximate areas of the WN, TMAZ, and HAZ. The height of the color represents the average parameter value of the zone. From the test results, the modulus of the weld area is between 30–70 GPa, the modulus of the TMAZ is the lowest, and the modulus of the HAZ is the highest. The distribution trend of elastic modulus is consistent with the result of the instrumented indentation testing [24]. The correlation between the distribution of plastic parameters and the region is not as good as the modulus of elasticity, and the plastic parameters generally show a decreasing trend from the weld nugget to both

sides. The distribution of yield strength and modulus in this paper are consistent with the distribution of microhardness in the literature [25]. The yield strength of the weld zone is between 75–115 MPa, and the difference in yield strength may be related to the distribution of residual stress. The parameter distribution presents an asymmetric W or M shape. The reason for the asymmetry is that there are forward and backward sides when the friction stir welding shoulder rotates. The asymmetry of the stirring action during the welding process causes the forward side to generate more heat than the backward side [22], which leads to differences in the properties of materials. It can be seen from Fig. 17 that the method developed in this paper obtains the material parameters of multiple micro-zones of the aluminum alloy friction stir welding material along the tensile direction, and then gives the average value of each zone. The reason for

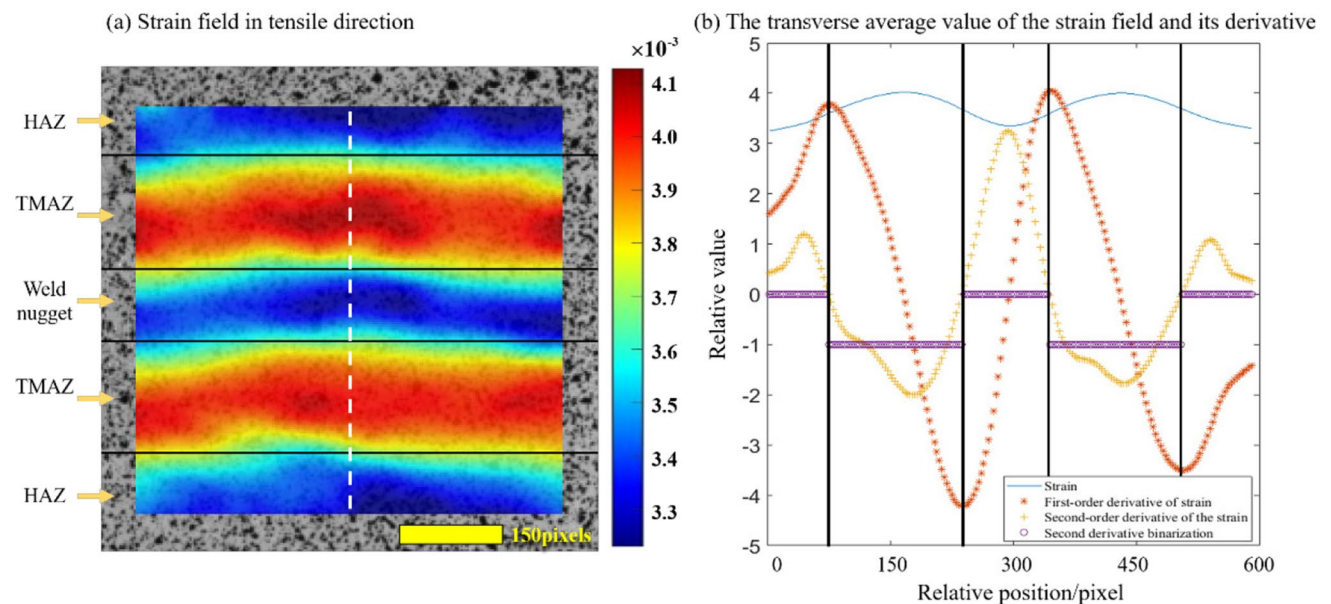
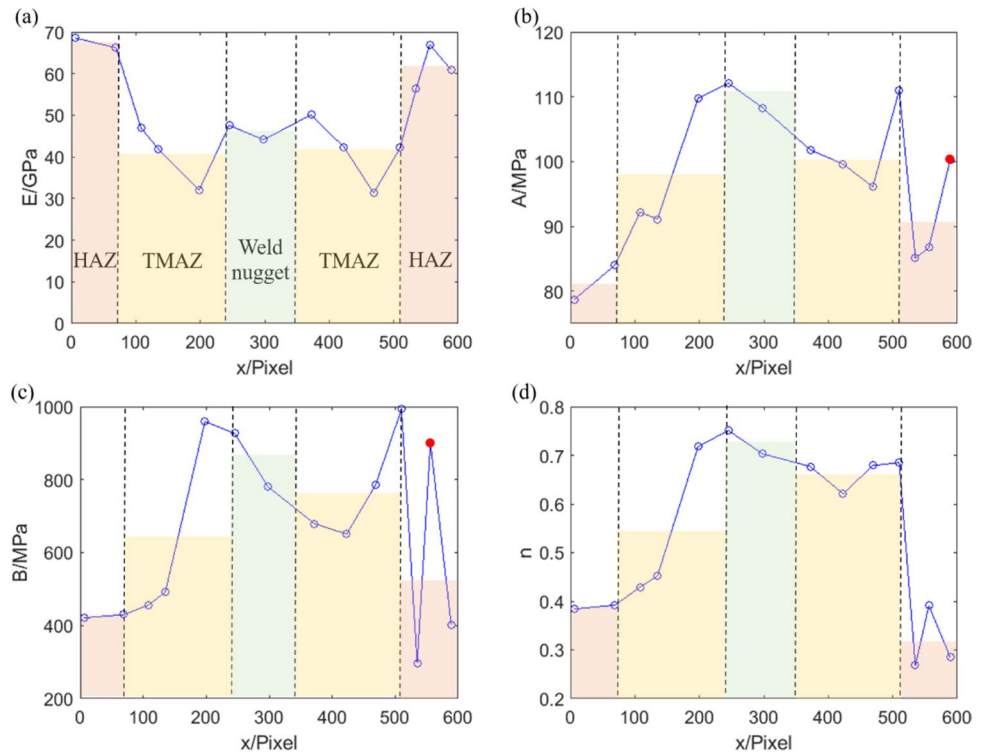


Fig. 16 Regional division results: (a) Division of strain field, (b) Relative values of strain, the first derivative of strain, and second derivative of strain

Fig. 17 The distribution of elastic–plastic parameters in the weld zone: (a) E; (b) A; (c) B; (d) n

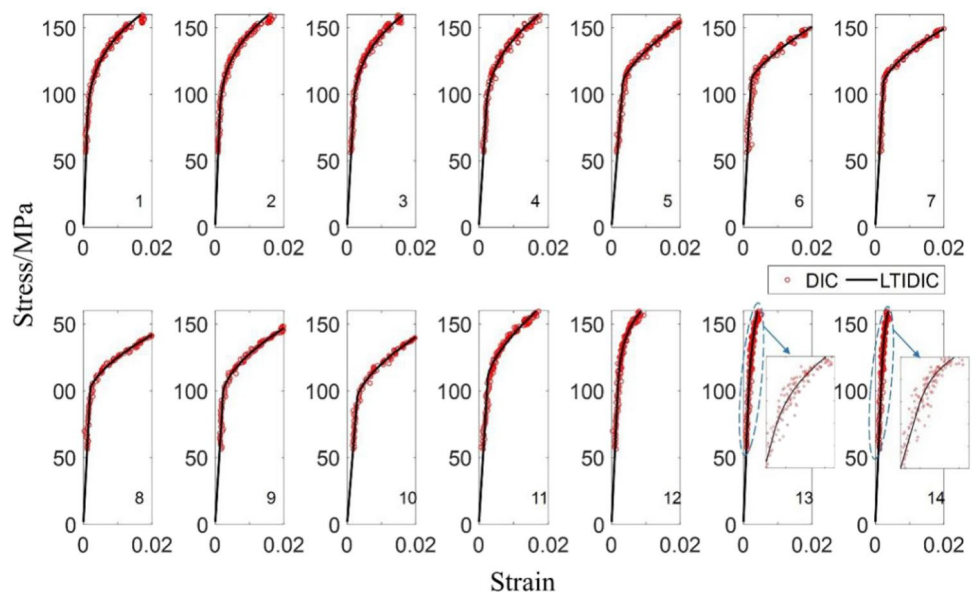


giving the average value of each zone is that the existing research divides the friction stir welding material into certain zones. In engineering applications, the areas with obvious differences in mechanical properties can be regarded as the same material parameters to simplify the calculation. The method proposed in this paper can obtain the material parameters of different local micro-zones selected in the speckle image, that is, this method can be applied to heterogeneous materials whose material parameters vary

continuously along the longitudinal direction, regardless of whether there are obvious boundaries.

In order to further verify the effectiveness of the method, the stress–strain curves of different regions were drawn according to the material elastic–plastic parameters identified by the LTIDIC algorithm and compared with the calculation results of the localized DIC method [11] which is a recognized method. The errors are within a small range, so the results are validated. When calculating the strain using

Fig. 18 Comparison of stress–strain curves of LTIDIC method and localized DIC method



the DIC method, the Ncorr software is used, the sub-region size is 45×45 pixels, the distance between the center points of the sub-region is 1 pixel, and the strain smoothing window size is 75×75 pixels. The comparison result is shown in Fig. 18. The 14 stress–strain curves respectively represent the stress–strain curves of the area centered on the 14 points in Fig. 17. The scattered data calculated by DIC fluctuates up and down around the inversion curve. The two have a good consistency. The average relative error between the two is 6.3929×10^{-4} , and the root mean square error is 1.1771×10^{-4} , proving the effectiveness and accuracy of the LTIDIC method. It can be seen from the enlarged images of the 13th and 14th subgraphs in the figure that the strain range in the stress–strain curve at the last two points is small (the maximum strain is less than 0.005) and the dispersion is relatively large, this is the reason for the abnormal points in the identification of the plastic parameter distribution (marked by the red dot in Fig. 18).

Conclusion

In order to improve the accuracy of multi-parameter measurement of heterogeneous materials and reduce potential manual intervention errors, this paper proposes a Local-micro-zone-wise Time-resolved Integrated Digital Image Correlation (LTIDIC) method, which can simultaneously inverse the elastic–plastic parameters of each characteristic region of welding joint through a uniaxial tensile experiment. The LTIDIC method is analyzed through numerical experiments, and the effects of the size of the localized subregion, the number of pictures, and the type of noise on the inversion results of the algorithm parameters are investigated. LTIDIC method to achieve accurate parameter inversion (error less than 5%) needs to ensure that the image sub-area is greater than $50 \text{ pixels} * 50 \text{ pixels}$, the number of images is greater than 30, and the method to further improve the accuracy (error less than 1%) is random sampling and calculate the sample mean. The proposed LTI-DIC method is used to automatically partition and inverse the parameters of the aluminum alloy friction stir welding weld area and obtain the distribution of the elastic–plastic parameters of the material in different areas of the weld. The elastic modulus distribution presents an asymmetric W-shape and the plastic parameters generally show a decreasing trend from the weld nugget to both sides. The LTIDIC method does not need to draw a stress–strain curve, but directly identifies the elastoplastic parameters of the material from the image. After getting the material parameters by the inversion according to the LTIDIC method, the stress–strain curve of each area drawn by the LTIDIC method is in good agreement with the result of the localized DIC method, which proves the effectiveness of the method. Due to the use of time series images, the LTIDIC method developed in this paper can obtain parameters such as

hardening coefficient and hardening exponent which are rarely obtained by I-DIC method [26–31]. For Young's modulus that can be obtained by both I-DIC and LTIDIC methods, the LTI-DIC measurement accuracy can reach 1% due to the reliability analysis and optimization of LTIDIC, which is more accurate than the multi-parameter inversion I-DIC [30]. The method developed in this paper has the following advantages:

- 1) It can automatically identify areas of heterogeneous materials with different mechanical properties in the tensile loading test, without manual division through fiber structure observation [31] or hardness test [32] before the tensile loading test, simplifying the process of measuring the elastic–plastic parameters of heterogeneous materials.
- 2) The LTIDIC method realizes that the parameter inversion error is less than 1% by analyzing the factors that affect parameter identification. It can effectively reduce the influence of random noise on the inversion of elastic–plastic parameters of heterogeneous materials and improve the accuracy of the results.
- 3) It can obtain multiple elastic–plastic parameter distributions including elastic modulus, yield strength, hardening coefficient, and hardening exponent simultaneously through a single tensile experiment.

Acknowledgements This work was financially supported by the National Natural Science Foundation of China [Grant Nos. 11972084], National Science and Technology Major Project (2017-VI-0003-0073) and Beijing National Science Foundation (1192014).

Declarations

Conflict of Interest The authors have no conflicts of interest to declare.

References

1. Mahoney MW, Rhodes CG, Flintoff JG, Bingel WH, Spurling RA (1998) Properties of friction-stir-welded 7075 T651 aluminum. *Metal and Mater Trans A* 29(7):1955–1964. <https://doi.org/10.1007/s11661-998-0021-5>
2. Fu RD, Zhang JF, Li YJ, Kang J, Liu HJ, Zhang FC (2013) Effect of welding heat input and post-welding natural aging on hardness of stir zone for friction stir-welded 2024–T3 aluminum alloy thin-sheet. *Mater Sci Eng, A* 559:319–324. <https://doi.org/10.1016/j.msea.2012.08.105>
3. Jones EM, Quintana EC, Reu PL, Wagner JL (2020) X-ray stereo digital image correlation. *Exp Tech* 44(2):159–174. <https://doi.org/10.1007/s40799-019-00339-7>
4. Pan R, Zhang G, Li S, Zheng X, Xu C, Fan Z (2021) Influence of the fracture process zone on fracture propagation mode in layered rocks. *J Petrol Sci Eng* 202:108524. <https://doi.org/10.1016/j.petrol.2021.108524>
5. Zappa E, Hasheminejad N (2017) Digital image correlation technique in dynamic applications on deformable targets. *Exp Tech* 41(4):377–387. <https://doi.org/10.1007/s40799-017-0184-3>

6. Zhang K, Qi F, Bao R, Xie J (2021) Physical reconstruction and mechanical behavior of fractured rock masses. *Bull Eng Geol Env* 80(6):4441–4457. <https://doi.org/10.1007/s10064-021-02206-5>
7. Boufaïda Z, Boisse J, André S, Farge L (2017) Mesoscopic strain field analysis in a woven composite using a spectral solver and 3D-DIC measurements. *Compos Struct* 160:604–612. <https://doi.org/10.1016/j.compstruct.2016.10.030>
8. Peng Y, Wu C, Gan J, Dong J (2018) Determination of the local constitutive properties of the welded steel joints using digital image correlation method. *Constr Build Mater* 171:485–492. <https://doi.org/10.1016/j.conbuildmat.2018.03.182>
9. Ramachandran S, Lakshminarayanan AK, Reed PAS, Dulieu-Barton JM (2019) Development of high-fidelity imaging procedures to establish the local material behavior in friction stir welded stainless steel joints. *Metals* 9(5):592. <https://doi.org/10.3390/met9050592>
10. Mani C, Balasubramani S, Karthikeyan R, Kannan S (2021) Digital Image Correlation of Tensile Properties for Monel 400/SS 316L Dissimilar Metal Welding Joints. *Materials* 14(6):1560. <https://doi.org/10.3390/ma14061560>
11. Bai R, Wei Y, Lei Z, Jiang H, Tao W, Yan C, Li X (2018) Local zone-wise elastic-plastic constitutive parameters of Laser-welded aluminium alloy 6061 using digital image correlation. *Opt Lasers Eng* 101:28–34. <https://doi.org/10.1016/j.optlaseng.2017.09.023>
12. Li G, Xu F, Sun G, Li Q (2014) Identification of mechanical properties of the weld line by combining 3D digital image correlation with inverse modeling procedure. *Int J Adv Manufac Technol* 74(5–8):893–905. <https://doi.org/10.1007/s00170-014-6034-x>
13. Pan B, Xie H, Guo Z, Hua T (2007) Full-field strain measurement using a two-dimensional Savitzky-Golay digital differentiator in digital image correlation. *Opt Eng* 46(3):033601. <https://doi.org/10.1117/1.2714926>
14. Gu J, Zhu F, Bai P, Lei D (2021) An optimized design for a field-of-view splitting-based long-gauge-length optical extensometer using two rhombic prisms. *Meas Sci Technol* 32(5):054001. <https://doi.org/10.1088/1361-6501/abd9f9>
15. Pan B, Tian L (2016) Advanced video extensometer for non-contact, real-time, high-accuracy strain measurement. *Opt Express* 24(17):19082–19093. <https://doi.org/10.1364/OE.24.019082>
16. Neggers J, Hoefnagels JP, Geers MGD, Hild F, Roux S (2015) Time-resolved integrated digital image correlation. *Int J Numer Meth Eng* 103(3):157–182. <https://doi.org/10.1002/nme.4882>
17. Piao M, Huh H, Lee I, Park L (2017) Characterization of hardening behaviors of 4130 Steel, OFHC Copper, Ti6Al4V alloy considering ultra-high strain rates and high temperatures. *Int J Mech Sci* 131:1117–1129. <https://doi.org/10.1016/j.ijmecsci.2017.08.013>
18. Jiang H, Lei Z, Bai R, Liu J, Guo Z, Dong H, Feng W (2021) Virtual Field Characterization for Ratcheting Effect Under Cyclic Loading. *Exp Mech* 1-17. <https://doi.org/10.1007/s11340-021-00709-6>
19. Pan B, Xie H, Wang Z (2010) Equivalence of digital image correlation criteria for pattern matching. *Appl Opt* 49(28):5501–5509. <https://doi.org/10.1364/AO.49.005501>
20. Park J, Yoon S, Kwon TH, Park K (2017) Assessment of speckle-pattern quality in digital image correlation based on gray intensity and speckle morphology. *Opt Lasers Eng* 91:62–72. <https://doi.org/10.1016/j.optlaseng.2016.11.001>
21. Lava P, Cooreman S, Debruyne D (2010) Study of systematic errors in strain fields obtained via DIC using heterogeneous deformation generated by plastic FEA. *Opt Lasers Eng* 48(4):457–468. <https://doi.org/10.1016/j.optlaseng.2009.08.013>
22. Ghosh M, Kumar K, Mishra RS (2011) Friction stir lap welded advanced high strength steels: Microstructure and mechanical properties. *Mater Sci Eng, A* 528(28):8111–8119. <https://doi.org/10.1016/j.msea.2011.06.087>
23. Blaber J, Adair B, Antoniou A (2015) Ncorr: open-source 2D digital image correlation matlab software. *Exp Mech* 55(6):1105–1122. <https://doi.org/10.1007/s11340-015-0009-1>
24. Fadaeifard F, Pakmanesh MR, Esfahani MS, Matori KA, Chicot D (2019) Nanoindentation analysis of friction stir welded 6061–T6 Al alloy in as-weld and post weld heat treatment. *Phys Met Metall* 120(5):483–491. <https://doi.org/10.1134/S0031918X1905003X>
25. Huang YX, Wan L, Lv ZL, Lv SX, Zhou L, Feng JC (2016) Microstructure and microhardness of aluminium alloy friction stir welds with heat treatment. *Sci Technol Weld Joining* 21(8):638–644. <https://doi.org/10.1080/13621718.2016.1152748>
26. Bertin M, Hild F, Roux S, Mathieu F, Leclerc H, Aimeidieu P (2016) Integrated digital image correlation applied to elastoplastic identification in a biaxial experiment. *J Strain Anal Eng Design* 51(2):118–131. <https://doi.org/10.1177/0309324715614759>
27. Baldi A (2014) Residual stress measurement using hole drilling and integrated digital image correlation techniques. *Exp Mech* 54(3):379–391. <https://doi.org/10.1007/s11340-013-9814-6>
28. Gazeau C, Gillibert J, Blond E, Geffroy PM, Richet N (2015) Experimental set up for the mechanical characterization of plane ITM membrane at high temperature. *J Eur Ceram Soc* 35(14):3853–3861. <https://doi.org/10.1016/j.jeurceramsoc.2015.06.026>
29. Mathieu F, Leclerc H, Hild F, Roux S (2015) Estimation of elastoplastic parameters via weighted FEMU and integrated-DIC. *Exp Mech* 55(1):105–119. <https://doi.org/10.1007/s11340-014-9888-9>
30. Dong J, Liu Z, Gao J (2017) Multi-parameter inversion and thermo-mechanical deformation decoupling using I-DIC. *Exp Mech* 57(1):31–39. <https://doi.org/10.1007/s11340-016-0203-9>
31. Wan L, Huang Y, Lv Z, Lv S, Feng J (2014) Effect of self-support friction stir welding on microstructure and microhardness of 6082–T6 aluminum alloy joint. *Mater Des* 55:197–203. <https://doi.org/10.1016/j.matdes.2013.09.073>
32. Wang DA, Lee SC (2007) Microstructures and failure mechanisms of friction stir spot welds of aluminum 6061–T6 sheets. *J Mater Process Technol* 186(1–3):291–297. <https://doi.org/10.1016/j.jmatprotec.2006.12.045>

Publisher's Note Springer Nature remains neutral with regard to jurisdictional claims in published maps and institutional affiliations.

Springer Nature or its licensor holds exclusive rights to this article under a publishing agreement with the author(s) or other rightsholder(s); author self-archiving of the accepted manuscript version of this article is solely governed by the terms of such publishing agreement and applicable law.